



AFRL-RY-WP-TR-2011-1245

HIGH EFFICIENCY PHOTOVOLTAIC AND PLASMONIC DEVICES

Gregory Sun

University of Massachusetts at Boston

JULY 2011

Final Report

Approved for public release; distribution unlimited.

See additional restrictions described on inside pages

STINFO COPY

**AIR FORCE RESEARCH LABORATORY
SENSORS DIRECTORATE
WRIGHT-PATTERSON AIR FORCE BASE, OH 45433-7320
AIR FORCE MATERIEL COMMAND
UNITED STATES AIR FORCE**

NOTICE AND SIGNATURE PAGE

Using Government drawings, specifications, or other data included in this document for any purpose other than Government procurement does not in any way obligate the U.S. Government. The fact that the Government formulated or supplied the drawings, specifications, or other data does not license the holder or any other person or corporation; or convey any rights or permission to manufacture, use, or sell any patented invention that may relate to them.

This report was cleared for public release by the USAF 66th Air Base Wing (66 ABW) Public Affairs Office (PAO) and is available to the general public, including foreign nationals. Copies may be obtained from the Defense Technical Information Center (DTIC) (<http://www.dtic.mil>).

AFRL-RY-WP-TR-2011-1245 HAS BEEN REVIEWED AND IS APPROVED FOR PUBLICATION IN ACCORDANCE WITH ASSIGNED DISTRIBUTION STATEMENT.

*//Signature//

RICHARD A. SOREF
Contract Monitor
Optoelectronic Technology Branch
Electromagnetics Technology Division

//Signature//

DAVID F. BLISS
Acting Branch Chief
Optoelectronic Technology Branch
Electromagnetics Technology Division

//Signature//

ROBERT V. McGAHAN
Technical Communications Adviser
Electromagnetics Technology Division
Sensors Directorate

This report is published in the interest of scientific and technical information exchange, and its publication does not constitute the Government's approval or disapproval of its ideas or findings.

*Disseminated copies will show “//Signature//” stamped or typed above the signature blocks.

REPORT DOCUMENTATION PAGE					Form Approved OMB No. 0704-0188	
<p>The public reporting burden for this collection of information is estimated to average 1 hour per response, including the time for reviewing instructions, searching existing data sources, gathering and maintaining the data needed, and completing and reviewing the collection of information. Send comments regarding this burden estimate or any other aspect of this collection of information, including suggestions for reducing this burden, to Department of Defense, Washington Headquarters Services, Directorate for Information Operations and Reports (0704-0188), 1215 Jefferson Davis Highway, Suite 1204, Arlington, VA 22202-4302. Respondents should be aware that notwithstanding any other provision of law, no person shall be subject to any penalty for failing to comply with a collection of information if it does not display a currently valid OMB control number. PLEASE DO NOT RETURN YOUR FORM TO THE ABOVE ADDRESS.</p>						
1. REPORT DATE (DD-MM-YY) July 2011		2. REPORT TYPE Final		3. DATES COVERED (From - To) 30 July 2009 – 08 July 2011		
4. TITLE AND SUBTITLE HIGH EFFICIENCY PHOTOVOLTAIC AND PLASMONIC DEVICES				5a. CONTRACT NUMBER FA8718-09-C-0045		
				5b. GRANT NUMBER		
				5c. PROGRAM ELEMENT NUMBER 61102F		
6. AUTHOR(S) Gregory Sun				5d. PROJECT NUMBER 2305		
				5e. TASK NUMBER HN		
				5f. WORK UNIT NUMBER 2305HN03		
7. PERFORMING ORGANIZATION NAME(S) AND ADDRESS(ES) University of Massachusetts at Boston Dept Grants & Adm Contracts 100 Morrissey Boulevard, Room 80 Boston, MA 02125-3300				8. PERFORMING ORGANIZATION REPORT NUMBER		
9. SPONSORING/MONITORING AGENCY NAME(S) AND ADDRESS(ES) Air Force Research Laboratory Sensors Directorate Wright-Patterson Air Force Base, OH 45433-7320 Air Force Materiel Command United States Air Force				10. SPONSORING/MONITORING AGENCY ACRONYM(S) AFRL/RHYA		
				11. SPONSORING/MONITORING AGENCY REPORT NUMBER(S) AFRL-RY-WP-TR-2011-1245		
12. DISTRIBUTION/AVAILABILITY STATEMENT Approved for public release; distribution unlimited.						
13. SUPPLEMENTARY NOTES HAFB PAO Case Number: 66ABW-2011-0590, cleared 17 May 2011. This report contains color.						
14. ABSTRACT This work focuses on laser diodes (LDs) that utilize the new silicon-germanium-tin technology capable of true monolithic integration on silicon. These miniature waveguided LDs would be key “enablers” for chip-scale networks of group IV active and passive components. In this work we have developed a rigorous analytical approach to the field enhancement in complex systems of coupled metallic nanoparticles. Our analysis confirms the fact that more complex metallic nanostructures do offer advantage over the single nanoparticles and provides a simple “engineering” explanation in which the large enhancement is achieved in a smaller “cavity” mode that is coupled to a larger “antenna” mode.						
15. SUBJECT TERMS Laser Diodes, Silicon-Germanium-Tin Technology						
16. SECURITY CLASSIFICATION OF:			17. LIMITATION OF ABSTRACT: SAR	18. NUMBER OF PAGES 36	19a. NAME OF RESPONSIBLE PERSON (Monitor) Richard A. Soref	
a. REPORT Unclassified	b. ABSTRACT Unclassified	c. THIS PAGE Unclassified			19b. TELEPHONE NUMBER (Include Area Code) N/A	

Table of Contents	Page #
List of Figures	iv
List of Tables	vi
Summary	1
I. Mid-IR GeSn/GeSiSn Multiple Quantum Well Laser	1
I.1 Brief overview	1
I.2 Band structure of GeSn/GeSiSn quantum wells	2
I.3 Carrier lifetime	5
I.4 Ge/Ge _{1-x-y} Si _x Sn _y conduction band structure	7
I.5 Conclusion	9
II. High efficiency thin-film crystalline Si/Ge tandem solar cell	9
II.1 Brief overview	9
II.2 Si/Ge tandem solar cell	10
II.3 Simulation method for the Si/Ge tandem cell	11
II.4 Results and discussion	14
II.3 Conclusions	16
III. Field enhancement by coupled metal nanoparticles	17
II.1 Brief overview	17
II.2 Theory of enhancement	17
II.3 Results and discussion	22
References	24
List of Symbols, Abbreviations, and Acronyms	26

List of Figures

Page

Figure 1	Band gaps of $\text{Ge}_{1-z}\text{Sn}_z$ at L , Γ , and X vs. Sn composition z , and (b) Γ -point band alignment between lattice matched $\text{Ge}_{1-x-y}\text{Si}_x\text{Sn}_y$ and $\text{Ge}_{0.9}\text{Sn}_{0.1}$ vs. the Sn composition y	4
Figure 2	Illustration of the GeSn/GeSiSn QW laser device on a lattice matched GeSn relaxed buffer on Si or SOI substrate along with its band alignment. This elongated mesa forms a strip channel waveguide.....	4
Figure 3	Radiative and Auger recombination lifetime as a function of temperature for the carrier density of $2 \times 10^{12}/\text{cm}^2$ in the $\text{Ge}_{0.9}\text{Sn}_{0.1}/\text{Ge}_{0.75}\text{Si}_{0.1}\text{Sn}_{0.15}$ MQW active region.	6
Figure 4	Optical confinement factor for the fundamental TM mode as a function of number of QWs in the active region of a $\text{Ge}_{0.9}\text{Sn}_{0.1}/\text{Ge}_{0.75}\text{Si}_{0.1}\text{Sn}_{0.15}$ QW laser with $\text{Ge}_{0.75}\text{Si}_{0.1}\text{Sn}_{0.15}$ cladding layers.....	7
Figure 5	Modal gain as a function of the injection current density at $T = 300\text{K}$ for the $\text{Ge}_{0.9}\text{Sn}_{0.1}/\text{Ge}_{0.75}\text{Si}_{0.1}\text{Sn}_{0.15}$ QW laser with different number of QWs.....	8
Figure 6	Illustration of (a) the Si-Ge tandem solar cell (b) the energy band diagram and carrier flow under solar irradiance.....	10
Figure 7	I-V characteristics at 500 suns of AM 1.5G solar irradiance for $V_t = 0$ and $g = 100/\Omega\text{cm}^2$	14
Figure 8	Open-circuit voltage and short-circuit current vs. number of suns concentration.	15
Figure 9	Efficiency of c-Si on c-Ge tandem PV cell vs. number of suns concentration for a range of the unit-area conductance of the tunnel junction. Also shown is the efficiency of an all-Si single junction PV cell of the same total thickness for comparison.....	16
Figure 10	Illustration of (a) the spherical coordinate system used to describe the metal sphere dipole polarized along z -axis and (b) the geometry of two coupled metal spheres that are separated by $r_0 = r_1 + r_2$	18

Figure 11	Illustration of (a) a metal nanosphere placed at the apex of a focused Gaussian beam with a numerical aperture characterized by the far-field half angle θ_a , and (b) the coupling of optical excitation into the dipole modes of both spheres and their subsequent coupling into the higher order modes.....	19
Figure 12	Field enhancement at the mid gap of two equal Au spheres in GaN vs. their radius at $\omega = \omega_1$. (Insert: frequency dependence of the mid-gap enhancement for the 5-nm gap with optimized sphere radius $a_{opt} = 33\text{nm}$.).....	22
Figure 13	Ratio of optimal field enhancement by two coupled spheres to that by a single sphere, $F_{C,opt}/F_{S,opt}$, and the frequency shift ω_{opt}/ω_1 to yield $F_{C,opt}$ vs. the gap. (Insert: maximum enhancement by a single sphere $F_{S,opt}$ achieved at a_{opt} vs. separation equal to half gap $d = g/2$.).....	23

List of Tables

Page

Table 1	Band parameters at various valleys used in the band alignment calculation.....3
---------	---

Summary

There are three parts in this report summarizing our research activities throughout this contract. First, we present modeling and simulation of a silicon-based group IV semiconductor injection laser diode in which the active region has a multiple quantum well structure formed with $\text{Ge}_{0.9}\text{Sn}_{0.1}$ quantum wells separated by $\text{Ge}_{0.75}\text{Si}_{0.1}\text{Sn}_{0.15}$ barriers. These alloy compositions are chosen to simultaneously yield a direct band gap for $\text{Ge}_{0.9}\text{Sn}_{0.1}$, and to provide type-I band alignment with $\text{Ge}_{0.75}\text{Si}_{0.1}\text{Sn}_{0.15}$ as well as a lattice match between them, so that the entire structure can be grown strain free upon a relaxed $\text{Ge}_{0.9}\text{Sn}_{0.1}$ buffer on a silicon substrate – a CMOS compatible process. Detailed analysis is performed for the type I band offsets, carrier lifetime, optical confinement, and modal gain. The carrier lifetime is found to be dominated by the spontaneous radiative process rather than the Auger process. The modal gain has a rather sensitive dependence on the number of quantum wells in the active region. The proposed laser is predicted to operate at 2.3 μm in the mid infrared at room temperature.

Second, we present our simulation result of a solar photovoltaic cell comprised of Si and Ge pn-junctions in tandem. With the assumption of anti-reflection at the front surface, we have shown that optimal solar cells favor a thin Si layer and a thick Ge layer with a thin tunneling hetero-diode placed in between. We predict efficiency ranging from 19 % to 28 % for AM1.5G solar irradiance concentrated from 1 ~ 1000 Suns for a cell with a total thickness ~100 μm .

Third, we present an analytical model that takes into account the coupling between the surface Plasmon modes in complex metal nanostructures. We apply this model to evaluate the field enhancement in the gap of two coupled Au metal spheres embedded in GaN dielectric and compare the result with that obtained by the single sphere. The results show additional improvement can be obtained in the gap depending on the width of the gap. This approach offers a clear physical insight for the enhancement and a straightforward method for optimization.

I. Mind-IR GeSn/GeSiSn Multiple Quantum Well Laser

I.1 Brief overview

This work focuses on laser diodes (LDs) that utilize the new silicon-germanium-tin technology [1,2] capable of true monolithic integration on silicon or SOI in a CMOS Fab. These miniature waveguided LDs would be key “enablers” for chip-scale networks of group IV active and passive components. This work addresses the issue of CW room-temperature operation at wavelengths beyond the 1.55 μm telecom band, wavelengths approaching the mid infrared. Our previous work on a 1.8 μm SiGeSn/GeSn/SiGeSn double heterostructure (DH) laser [3] showed that Auger recombination was a limiting process that constrained the LD to operate at temperatures around 200K. By contrast, the multiple-quantum-well (MQW) approach proposed in this paper offers suppression of Auger recombination to the extent that carrier lifetime is dominated by spontaneous radiative recombination. This MQW offers a lower density of states in the active layers, resulting in a lower electron-and-hole concentration

required for population inversion. The MQW is significantly better than the DH because of its lower threshold and higher temperature of operation, including 300K.

Here we present design-and-simulation results on a waveguided electrically injected PIN MQW diode in which the active region has GeSn layers as QWs and SiGeSn ternary layers as barriers as well as the cladding regions. The compositions of GeSn and SiGeSn are chosen in such a way that not only they form type-I band alignment at the Γ -point but also are lattice matched. The laser would be situated on a relaxed buffer layer of GeSn-upon-silicon or SOI [4] whose lattice parameter is the same as that of the GeSn/SiGeSn laser, hence the entire laser structure is unstrained. The band-to-band MQW laser diode simulated in this paper has an emission wavelength of 2.3 μ m in the mid infrared. The results reported here compliment the previous simulations of a 1.55-mm GeSn-quantum-well laser [5], a strained GeSn/GeSiSn QW laser [6], and a Terahertz Ge/SiGeSn quantum cascade laser [7]. Our strain-free MQW should be easier to implement than the strained prior-art QW lasers [5, 6]. The analysis of carrier lifetime presented here includes recombination effects due to radiative and non-radiative Auger processes. Our result indicates that this MQW laser would operate at room temperature.

I.2 Band structure of GeSn/GeSiSn quantum wells

Energy-band theory [8] and FTIR absorption experiments [9] have indicated that the bandgap of unstrained crystalline GeSn makes a transition from indirect to direct as the percent of α -Sn is increased. Since band offsets between ternary Sn-containing alloys and Si or Ge are not known experimentally, we follow the assumptions made in Ref. [1] and calculate the conduction band minima for the lattice- matched heterostructure consisting of $\text{Ge}_{1-z}\text{Sn}_z$ and a ternary $\text{Ge}_{1-x-y}\text{Si}_x\text{Sn}_y$ based on Jaros' band offset theory [10], which is in good agreement with experiment for many heterojunction systems. For example, this theory predicts an average valence band offset, $\Delta E_{v,av} = 0.48\text{eV}$ for a Ge/Si hetero-interface (higher energy on the Ge side), close to the accepted value of $\Delta E_{v,av} = 0.5\text{eV}$. The basic ingredients of our band alignment calculation are the average (between heavy, light, and split-off hole bands) valence band offset between the two materials and the compositional dependence of the band structure of the ternary alloy. For the Ge/ α -Sn interface Jaros' theory predicts $\Delta E_{v,av} = 0.69\text{eV}$ (higher energy on the α -Sn side). Thus, relative to the average valence band of Ge, the average valence band position for $\text{Ge}_{1-x-y}\text{Si}_x\text{Sn}_y$ is simply a linear interpolation

$$E_{v,av}(\text{Ge}_{1-x-y}\text{Si}_x\text{Sn}_y) = -0.48x + 0.69y. \quad (1)$$

Similarly, with these spin-orbit splitting values $\Delta_{so}(\text{Ge}) = 0.295\text{eV}$, $\Delta_{so}(\text{Si}) = 0.043\text{eV}$, $\Delta_{so}(\text{Sn}) = 0.800\text{eV}$ [12], the spin-orbit splitting for $\text{Ge}_{1-x-y}\text{Si}_x\text{Sn}_y$ is

$$\Delta_{so}(\text{Ge}_{1-x-y}\text{Si}_x\text{Sn}_y) = 0.295(1 - x - y) + 0.043x + 0.800y. \quad (2)$$

The top of the valence band for $\text{Ge}_{1-x-y}\text{Si}_x\text{Sn}_y$ can then be determined as

$$E_v(\text{Ge}_{1-x-y}\text{Si}_x\text{Sn}_y) = E_{v,av}(\text{Ge}_{1-x-y}\text{Si}_x\text{Sn}_y) + \frac{\Delta_{so}(\text{Ge}_{1-x-y}\text{Si}_x\text{Sn}_y)}{3}. \quad (3)$$

The minima of the conduction band at points L and Γ can then be calculated by evaluating the compositional dependence of the band gaps of the ternary alloy as

$$E(\text{Ge}_{1-x-y}\text{Si}_x\text{Sn}_y) = E_{\text{Ge}}(1-x-y) + E_{\text{Si}}x + E_{\text{Sn}}y - b_{\text{GeSi}}(1-x-y)x - b_{\text{GeSn}}(1-x-y)y - b_{\text{SiSn}}x \quad (4)$$

where E_{Ge} , E_{Si} , and E_{Sn} are the bandgap of Ge, Si, and α -Sn, respectively, at those points, and the bowing parameters b_{GeSi} , b_{GeSn} , b_{SiSn} have been discussed in Refs. [13,14]. These values at L and Γ points have been given in Table 1.

Table 1. Band parameters at various valleys used in the band alignment calculation [12-14].

Valley	E_{Ge} [eV]	E_{Si} [eV]	E_{Sn} [eV]	b_{GeSi} [eV]	b_{GeSn} [eV]	b_{SiSn} [eV]
L	0.66	2.0	0.14	0.0	-0.11	0.0
Γ	0.795	4.06	-0.413	0.21	1.94	13.2

Finally, for the indirect conduction band minimum near the X -point, Weber and Alonso find

$$E_X(\text{Ge}_{1-x}\text{Si}_x) = 0.931 + 0.018x + 0.206x^2 \quad (5)$$

(in eV) for $\text{Ge}_{1-x}\text{Si}_x$ alloys [14]. On the other hand, the empirical pseudopotential calculations of Chelikovsky and Cohen place this minimum at 0.90 eV in α -Sn, virtually the same as its value in pure Ge [15]. We thus assume that the position of this minimum in ternary $\text{Ge}_{1-x-y}\text{Si}_x\text{Sn}_y$ alloys is independent of the Sn concentration y , and thus is also given by Eq.(5). Obviously, the calculation of band structures outlined above is an approximation that is subject to experimental corrections as more measurements become available. This implies that the compositions of $\text{Ge}_{1-z}\text{Sn}_z$ and $\text{Ge}_{1-x-y}\text{Si}_x\text{Sn}_y$ are necessarily adjusted in the QW structure to arrive at the band structure that is being proposed here. But it should be pointed out that the laser behavior depends only on the band structure, and the results obtained in this design should be valid albeit at slightly different binary and ternary compositions.

The α -Sn composition dependence of the conduction band gaps for $\text{Ge}_{1-z}\text{Sn}_z$ at the three valleys L , Γ , and X is first calculated using Eqs.(4) and (5) to establish the crossing point where the Γ -point band gap drops below that of the L -point. Figure 1(a) shows that for α -Sn composition greater than $z \geq 6\%$, $\text{Ge}_{1-z}\text{Sn}_z$ becomes direct band gap. We thus choose $\text{Ge}_{0.9}\text{Sn}_{0.1}$ to be the QW layer with a direct band gap of $E_g = 0.505\text{eV}$. Fixing at this composition $\text{Ge}_{0.9}\text{Sn}_{0.1}$, we then looked for a lattice matched $\text{Ge}_{1-x-y}\text{Si}_x\text{Sn}_y$ that can be used as barriers that form type-I band alignment with $\text{Ge}_{0.9}\text{Sn}_{0.1}$. Such a simultaneous requirement for lattice constant and band alignment can be satisfied by the additional degree of freedom in the $\text{Ge}_{1-x-y}\text{Si}_x\text{Sn}_y$ where both x and y can be tuned. Using Vegard's law for the lattice constant of $\text{Ge}_{1-x-y}\text{Si}_x\text{Sn}_y$, the lattice constant of $\text{Ge}_{1-x-y}\text{Si}_x\text{Sn}_y$

$$a(\text{Ge}_{1-x-y}\text{Si}_x\text{Sn}_y) = a_{\text{Ge}}(1-x-y) + a_{\text{Si}}x + a_{\text{Sn}}y \quad (6)$$

where the lattice constants $a_{\text{Ge}} = 5.64613 \text{ \AA}$, $a_{\text{Si}} = 5.43095 \text{ \AA}$, and $a_{\text{Sn}} = 6.48920 \text{ \AA}$ for Ge, Si, and α -Sn [11], respectively, we can vary the Si and α -Sn compositions simultaneously to yield exactly the lattice constant of $\text{Ge}_{0.9}\text{Sn}_{0.1}$. Adding the band gaps to the top of the valence band Eq.(3), we obtain the band alignment between at the Γ -point as shown in Figure1(b)

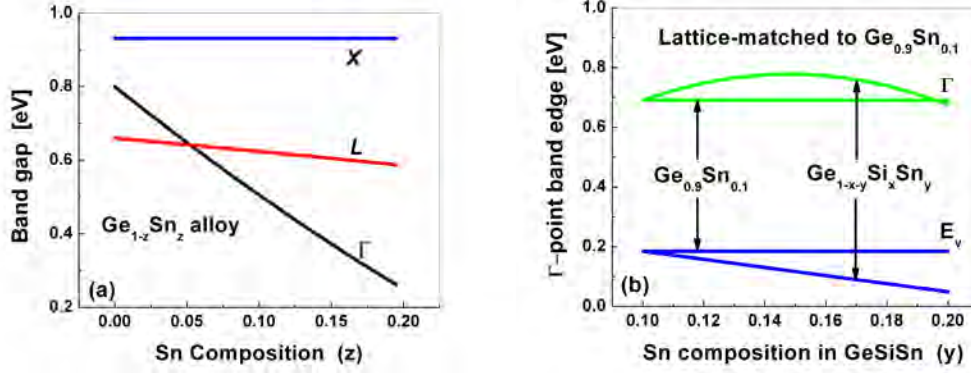


Figure1. (a) Band gaps of $\text{Ge}_{1-z}\text{Sn}_z$ at L , Γ , and X vs. Sn composition z , and (b) Γ -point band alignment between lattice matched $\text{Ge}_{1-x-y}\text{Si}_x\text{Sn}_y$ and $\text{Ge}_{0.9}\text{Sn}_{0.1}$ vs. the Sn composition y .

There is a wide range of Sn composition $0.1 < y < 0.19$ in which the ternary $\text{Ge}_{1-x-y}\text{Si}_x\text{Sn}_y$ forms type-I confinement with $\text{Ge}_{0.9}\text{Sn}_{0.1}$, i.e., both elections and holes are confined in the $\text{Ge}_{0.9}\text{Sn}_{0.1}$ QWs by the $\text{Ge}_{1-x-y}\text{Si}_x\text{Sn}_y$ barriers. In particular, we choose the barriers with the composition $\text{Ge}_{0.75}\text{Si}_{0.1}\text{Sn}_{0.15}$ that gives the largest conduction band offset of $\Delta E_{c,\Gamma} = 88 \text{ meV}$, and that of valence band $\Delta E_v = 68 \text{ meV}$ as shown in Fig. 1(b). The laser device shall be grown on a relaxed $\text{Ge}_{0.9}\text{Sn}_{0.1}$ buffer on a Si substrate to ensure that the entire structure is strain free as illustrated in Figure 2.

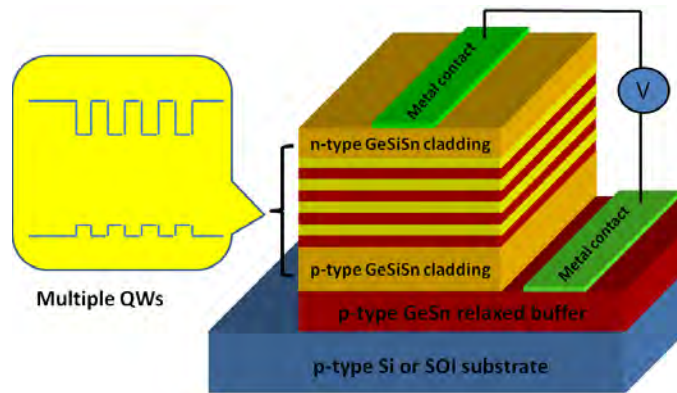


Figure 2. Illustration of the GeSn/GeSiSn QW laser device on a lattice matched GeSn relaxed buffer on Si or SOI substrate along with its band alignment. This elongated mesa forms a strip channel waveguide.

I.3 Carrier lifetime

The proposed laser device has MQWs in its active region. Since the compositions of Sn and Si are relatively small in comparison with that of Ge for either QW or barrier layers, we shall use Γ -point Ge parameters in the following calculations. The quantum confinement leads to energy subbands in both conduction and valence bands. The energy levels of these subbands can be calculated by solving the one-dimensional Schrödinger equation following the envelope function approximation [16]. The laser device under consideration has a forward-biased PIN structure where the active MQW region is undoped. The band-to-band lasing transitions occur as stimulated emissions triggered by recombination of electron-hole pairs that are injected into this region. The analysis proceeds as follows. For a given carrier density, we can derive quasi Fermi levels at a specific temperature (T) for electrons in the conduction band (E_{fc}), and for light holes (LHs) and heavy holes (HHs) in the valence band (E_{fv}). However, only the electron-HH pair recombination contributes to lasing transitions since the ground-state HH subband lies lower in energy than that of the LH subband. The structure that we have calculated was chosen to have 20nm $\text{Ge}_{0.9}\text{Sn}_{0.1}$ QWs that are separated by 20nm $\text{Ge}_{0.75}\text{Si}_{0.1}\text{Sn}_{0.15}$ barriers. The energy separation between the ground-state electron and HH subbands has been determined to be $E_q = 0.541\text{eV}$, which is 36meV larger than the $\text{Ge}_{0.9}\text{Sn}_{0.1}$ band gap (0.505eV) due to the quantum confinement.

In order to estimate the carrier lifetime, it is necessary to calculate the radiative as well as Auger recombination rate in the MQW active region. The radiative process is spontaneous consisting of electron-heavy hole (e-hh) as well as electron-light hole (e-lh) recombination. The spontaneous emission rate per unit area in the energy interval $E \rightarrow E + dE$ due to the e-hh process can be calculated as [16],

$$R_{sp,e-hh} = \frac{\bar{n}e^2m_r|M_b|^2}{\pi^2m_0^2\varepsilon_0\hbar^4c^3d} \int_{E_q}^{\infty} E f_c(E_e)f_v(E_{hh})dE \quad (7)$$

where e is the electron charge, m_0 the free electron mass, ε_0 the permittivity of vacuum, \hbar the Planck constant, c the speed of light in vacuum, \bar{n} the index of refraction, d the QW width, and $|M_b|^2$ the average matrix element for the Bloch states [16]. The occupation probabilities at the states that are separated by a photon energy E with the same \mathbf{k} in the reciprocal space are

$$\begin{aligned} f_c(E_e) &= \left[1 + \exp \left(\frac{E_e - E_{fc}}{k_B T} \right) \right]^{-1} \\ f_v(E_{hh}) &= \left[1 + \exp \left(\frac{E_{fv} - E_{hh}}{k_B T} \right) \right]^{-1} \end{aligned} \quad (8)$$

respectively, where k_B is the Boltzmann constant, and the electron and hole energies in the conduction and valence subbands

$$\begin{aligned} E_e &= \frac{m_r}{m_e} (E - E_q) \\ E_{hh} &= \frac{m_r}{m_{hh}} (E - E_q) \end{aligned} \quad (9)$$

are computed through the reduced effective mass

$$m_r = \frac{m_e m_{hh}}{m_e + m_{hh}} \quad (10)$$

in which m_e and m_{hh} are the electron and HH effective mass, respectively. Obviously, the spontaneous emission rate $r_{sp,e-lh}(E)dE$ for the radiative e-lh process can be obtained similarly. The total spontaneous emission rate per unit area can be obtained as

$$R_{rad} = R_{sp,e-hh} + R_{sp,e-lh} \quad (11)$$

The radiative lifetime can then be obtained by $\tau_{rad} = n/R_{rad}$ where n is the area carrier density. The result for the area carrier density of $n = 2 \times 10^{12}/\text{cm}^2$, corresponding to a carrier concentration of $10^{18}/\text{cm}^3$ in QW layers for the well thickness of $d = 20\text{nm}$, is shown in Fig.3 for a range of temperature. It can be seen that the radiative lifetime for a fixed carrier density is rather insensitive to temperature change, showing a slight increase with the temperature.

This radiative carrier lifetime can be shown to be much shorter than that of the Auger process where the recombination of an electron-hole pair takes place by transferring energy and momentum to a third particle which could be either an electron or a hole. For comparison, we have also estimated the Auger lifetime by following the calculation procedure outlined in Ref. [16]. The result for the same area carrier density of $n = 2 \times 10^{12}/\text{cm}^2$ determined by the Auger process is shown in Fig. 3. Clearly the Auger lifetime decreases rapidly with the increase of temperature, but even at $T = 300\text{K}$, it remains longer than that of the radiative process. We therefore conclude the spontaneous radiative recombination is the dominant process in determining the carrier lifetime. In comparison with the DH laser that we have simulated earlier [3], this represents a significant improvement which leads to its potential room temperature operation.

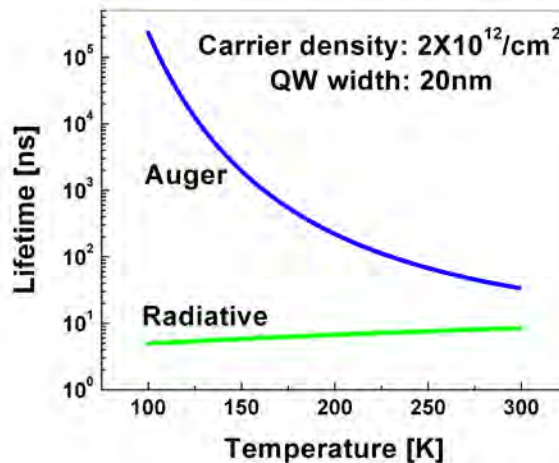


Figure 3. Radiative and Auger recombination lifetime as a function of temperature for the carrier density of $2 \times 10^{12}/\text{cm}^2$ in the $\text{Ge}_{0.9}\text{Sn}_{0.1}/\text{Ge}_{0.75}\text{Si}_{0.1}\text{Sn}_{0.15}$ MQW active region.

I.4 Ge/Ge_{1-x-y}Si_xSn_y conduction band structure

In contrast to their advantage of having longer carrier lifetime, single QW lasers typically have very small optical confinement factor in comparison with that of DH lasers because their active regions are too thin relative to the lasing wavelength. Fortunately, the MQW structure offers a practical solution to the mode-overlap problem by increasing the effective thickness of the active region. Figure 4 shows the optical confinement factor for the fundamental TM mode of the Ge_{0.9}Sn_{0.1}/Ge_{0.75}Si_{0.1}Sn_{0.15} QW lasers with a range of QW numbers whose active regions consist of 20nm Ge_{0.9}Sn_{0.1} QWs that are separated by 20nm Ge_{0.75}Si_{0.1}Sn_{0.15} barriers, and where the active region is cladded by thick Ge_{0.75}Si_{0.1}Sn_{0.15} layers. The confinement factor Γ , defined as the spatial overlap integral of the TM₀ mode profile with the gain profile, increases from 0.003 for a single QW to 0.90 for 35 QWs.

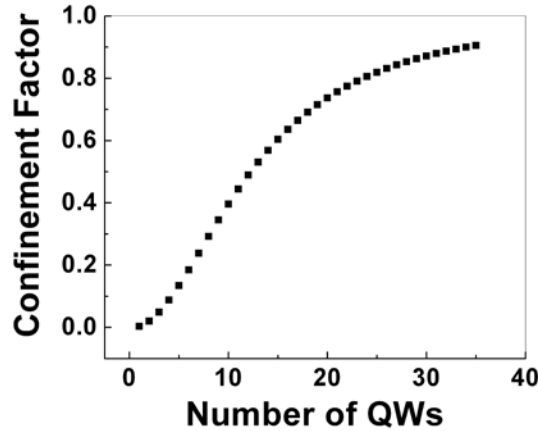


Figure 4. Optical confinement factor for the fundamental TM mode as a function of number of QWs in the active region of a Ge_{0.9}Sn_{0.1}/Ge_{0.75}Si_{0.1}Sn_{0.15} QW laser with Ge_{0.75}Si_{0.1}Sn_{0.15} cladding layers.

For a given injected area carrier density $n = p$, we can calculate the optical gain at a photon energy E due to e-hh recombination as [16]

$$g = \frac{e^2 m_r |M_b|^2}{\epsilon_0 m_0^2 c \hbar n E d} [f_c(E_e) + f_v(E_{hh}) - 1]. \quad (12)$$

Taking into account the mode confinement, we have evaluated the model gain which is given as Γg , the product of the mode confinement factor and the optical gain. The carriers that are responsible for the modal gain are excited by external pumping. A preferred pumping method is current injection capable of sustaining the carriers characterized by their lifetime. At lasing threshold where the stimulated emission is just about to take place, the injection current density J_{th} is related to the number of QWs (n_{qw}) and to the carrier recombination rate per QW (R_{rad}) as $J_{th} = en_{qw}R_{rad}$ when the spontaneous radiative recombination process is dominant. The result of modal gain at the photon energy $E = E_q = 0.541\text{eV}$ ($\lambda = 2.3\ \mu\text{m}$) as a function the injection current density is shown in Figure 5 at $T = 300\text{K}$ for the Ge_{0.9}Sn_{0.1}/Ge_{0.75}Si_{0.1}Sn_{0.15}

QW laser with different numbers of QWs, n_{qw} , but all of the lasers have 20nm QWs and 20nm barriers.

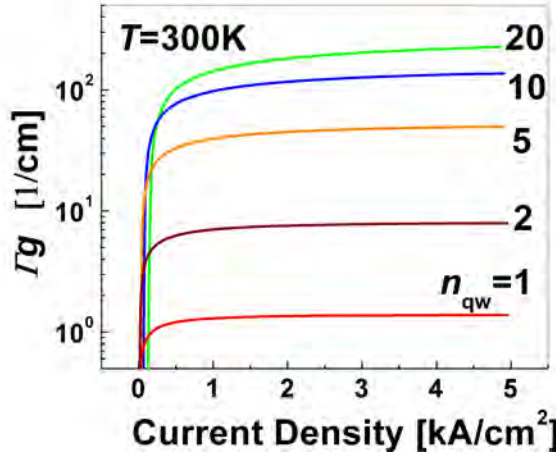


Figure 5. Modal gain as a function of the injection current density at $T = 300\text{K}$ for the $\text{Ge}_{0.9}\text{Sn}_{0.1}/\text{Ge}_{0.75}\text{Si}_{0.1}\text{Sn}_{0.15}$ QW laser with different number of QWs.

Initially, the modal gain increases rapidly with pumping current as the injected carriers start to establish the population inversion between the ground-state electron and HH subbands and to produce the optical gain g at the photon energy that is equal to the energy separation between the bottom of the ground-state electron subband and the top of the ground-state HH subband. As the pumping current continues to increase, the occupation status of electrons and HHs at those extreme locations of the involved subbands will no longer change, i.e. $f_c(E_e) = 1$, and $f_v(E_{hh}) = 1$ in Eq.(12) indicating that the maximum population inversion has been established. For different number of QWs, the modal gain reaches different saturation values. This is a direct result of the mode confinement factor as shown in Fig.4. The modal gain of a laser must be sufficient to compensate for the various losses in the device such as the free carrier absorption and imperfect mirror reflectivity. Figure 5 shows that an adequate number of QWs must be designed to overcome a certain level of losses. For instance, 20 QWs are needed to provide modal gain of just over 100/cm. In general, active regions consisting of a larger number of QWs are more capable of providing higher modal gains. This obviously creates strict demands upon the structural growth that must offer very fine control of layer thicknesses as well as uniformity of the layer thickness and alloy compositions. Fortunately, the recent result on epitaxial techniques exhibiting very fine control of GeSiSn alloy layers has indeed opened a pathway to developing GeSn QW lasers [17]. The proposed laser design utilizes a lattice matched structure that conveniently avoids the situation of strain development as more QWs are deposited – a welcome factor for the device growth.

It may be desired to increase the laser's emission wavelength into the 3 to 5 μm band (the atmospheric transmission window). Then it is necessary to increase the Sn content of the QWs beyond 10% and to change the barrier composition to lattice-match the new QWs. Having done this for $\lambda = 3.5 \mu\text{m}$, we found that the well/barrier conduction-band offset decreased to about 20 meV, a value not sufficient for good confinement of electrons. However, this offset problem may be solvable by employing SiGeSn QWs along with ternary barriers.

I.5 Conclusion

We propose a simple group-IV laser made of a PIN-diode $\text{Ge}_{0.94}\text{Sn}_{0.06}/\text{Ge}_{0.75}\text{Si}_{0.15}\text{Sn}_{0.1}$ MQW active region wherein the direct-gap $\text{Ge}_{0.9}\text{Sn}_{0.1}$ QWs are confined by $\text{Ge}_{0.75}\text{Si}_{0.1}\text{Sn}_{0.15}$ barrier layers. The optical channel-waveguide confinement is provided by the same ternary $\text{Ge}_{0.75}\text{Si}_{0.1}\text{Sn}_{0.15}$ cladding layers of large thickness. The compositions of both the QW and the barrier/cladding layers are determined to yield lattice matching and type-I band alignment between them. The laser structure would be grown on a relaxed $\text{Ge}_{0.9}\text{Sn}_{0.1}$ buffer on either Si or SOI, hence the device is strain free. Both radiative and nonradiative Auger processes are included in the simulation of carrier recombination rate. It is shown that the carrier lifetime is determined by the radiative process rather than the Auger process. In particular, we have analyzed a MQW laser with an active region consisting of 20nm $\text{Ge}_{0.94}\text{Sn}_{0.06}$ wells and 20nm $\text{Ge}_{0.75}\text{Si}_{0.15}\text{Sn}_{0.1}$ barriers that are optically confined by thick $\text{Ge}_{0.75}\text{Si}_{0.1}\text{Sn}_{0.15}$ cladding layers. The quantum confinement leads to an energy separation between the ground-state electron and HH subbands equal to 0.541eV, which yields a lasing wavelength of 2.3 μm . Optical confinement varies over a wide range depending on the number of QWs employed in the active region. Modal gain is calculated as a function of injection current density for a range of QW numbers at room temperature. For a laser with 20 QWs, the optical confinement factor reaches 0.74 and the modal gain can exceed 200/cm for a pumping current density under 3kA/cm², which is sufficient to compensate for losses in mid IR semiconductor lasers. It can be concluded that the implementation of this laser will lead to the first electrically injected group-IV near/mid-IR laser capable of operating at room temperature, a laser that is integrated on Si or SOI.

II. High efficiency thin-film crystalline Si/Ge tandem solar cell

II.1 Brief overview

The relatively weak power of sunlight fundamentally limits the power output from a solar cell, which in turn increases its cost per unit power delivered. Solar-concentration systems have the potential to reduce the cost of solar-to-electricity conversion by using inexpensive lenses or mirrors to direct highly concentrated solar flux onto a small-area solar cell. But the “merit” of a photovoltaic (PV) cell depends upon the PV material manufacturing costs as well as the cell’s efficiency. Solar cells made of III-V semiconductor compounds have higher efficiency but are typically more expensive than those made of silicon, motivating a group IV solution. In this paper, we propose a solar concentrator that uses a tandem solar cell made of group-IV PV material in which a Si junction is stacked on top of a Ge junction. Such a solar structure is capable of delivering significantly higher efficiency than the single-junction all-Si solar cell.

Crystalline Ge is in many ways a better solar photovoltaic (PV) material than crystal Si because Ge’s optical absorption has a wider spectral overlap with the solar irradiance spectrum (Ge covers the 300 to 1600 nm wavelength range compared to the 300 to 1060 nm coverage of Si), Ge has a steeper absorption edge than Si since its bandgap is almost direct at 0.66 eV, and the optical absorption coefficients of Ge are generally higher than those of Si in the range of interest. In addition, Ge is known to be an excellent bottom junction material in a multi-junction solar cell. For these reasons, we are proposing a tandem PV cell comprised of a c-Si

pn-junction on top of a c-Ge pn-junction with a tunneling hetero-diode in between. Matching the photocurrent in Ge to the photocurrent in Si quickly points to a cell structure consisting mostly of Ge with very thin Si. Our simulations predict conversion efficiencies that are significantly higher than those of corresponding thin-film stand-alone Si [18-22]. The PV efficiency calculated here ranges from 19 % to 28 % for AM1.5G solar irradiance [23] concentrated from 1 to ~ 1000 Suns. The result is for a flat uniform-planar cell, and its efficiency can be further increased via techniques such as surface passivation and light trapping treatments.

The solar device proposed here has technical and technological issues. In this paper we investigate the former but not the latter. One technological issue is large-area low-cost manufacturing which usually includes the use of a low-cost “foreign” substrate such as glass or ceramic (preferably not Si). Another issue is defects at the heterointerface that arise because of the Si/Ge lattice mismatch. Although technological issues of producing the Si/Ge heterostructure remain challenging, high-quality c-Si has already been grown successfully on c-Ge [24,25] with dislocations at the interface, together with some unwanted travel of Si atoms several nanometers into the Ge. Our goal is to point the way (with theory) to the development of practical high-efficiency cells.

II.2 Si/Ge tandem solar cell

Figure 6 (a) shows the cross-sectional side view of our proposed thin-film c-Si on c-Ge PV cell whose overall thickness is less than ~ 100 μm . Since the Si has a wider bandgap than that of Ge, it is necessary in the Si/Ge tandem cell to have Si junction in front of the Ge junction. Both junctions have a 1- μm -thick “emitter” region with p-type doping of $5 \times 10^{17} \text{ cm}^{-3}$. The “base” region thickness is 6 μm for the Si junction and is 90 μm for the Ge junction. Both bases have n-type doping of 10^{18} cm^{-3} . The tunneling diode at the Si-Ge interface has a thickness of ~ 100 nm with n-type Si and p-type Ge very heavily doped. The energy band diagram of this tandem cell is illustrated in Figure 6 (b) showing the carrier flow generated by solar irradiance.

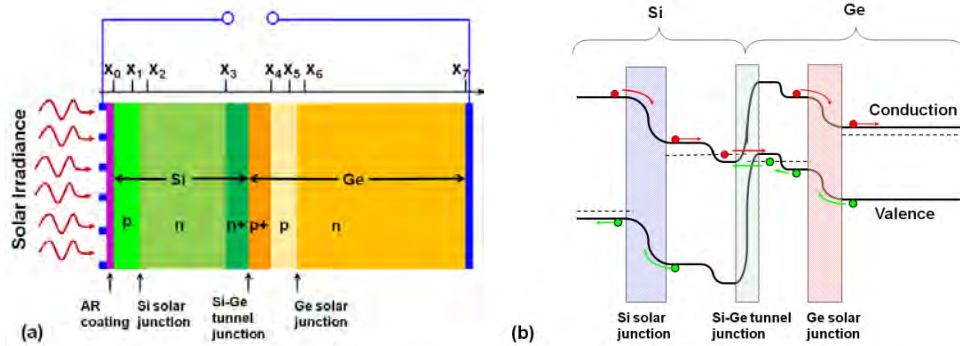


Figure 6. Illustration of (a) the Si-Ge tandem solar cell (b) the energy band diagram and carrier flow under solar irradiance.

The predictions of the solar cell performance are made based on the following assumptions: (1) the well known experimental optical-and-infrared absorption spectra of Si and

Ge [26] can be used here because the materials are mono crystalline; (2) an anti- reflection (AR) coating at the front is employed, thus the efficiency figures cited do not include the 30 % reflection loss at air-to-Si; (3) front-surface metal-finger contacts cover only a tiny fraction of the cell area , but perfect Ohmic contact at the back surface is assumed; (4) series resistance of the PV cell is neglected, but the resistive effect of the tunnel junction is included; (5) defects developed due to lattice mismatch is confined at the Si-Ge interface. The last assumption ensures that the defects will not significantly reduce the minority carrier lifetimes in the active regions of the solar cell. By confining the defects at the Si-Ge interface, their impact is limited only to the tunneling diode. One major effect of these defects is to introduce carrier-recombination centers within the tunneling diode which can actually serve to increase the tunneling current – a potentially positive impact on the current transport behavior.

II.3 Simulation method for the Si/Ge tandem cell

Let us consider that a specific solar spectral irradiance $I(\lambda)$ (the solar intensity per unit wavelength interval at a given wavelength λ) is incident on the AR-coated front surface of the solar cell. In each of the solar junctions located in Si and Ge layers, the solar current is generated in three regions, two from the neutral regions and one from the depletion region, a current that can be determined by obtaining the distribution of excess minority carriers in those regions under solar irradiance. Within each of the neutral regions, the number of excess carriers generated at each wavelength λ per unit wavelength interval obeys the steady-state continuity equation with the approximation of zero electric field outside of the depletion region. We shall use the p-type neutral region of the Si layer $x_0 < x < x_1$ to illustrate the procedure for obtaining the excess carriers in any of the four neutral regions of the two junctions. The steady-state continuity equation for $x_0 < x < x_1$ can be written for excess electron concentration $\Delta n_\lambda(x)$ under solar spectral irradiance $I(\lambda)$ as

$$D_{e,\text{Si}} \frac{\partial^2 \Delta n_\lambda(x)}{\partial x^2} - \frac{\Delta n_\lambda(x)}{\tau_{e,\text{Si}}} + G_\lambda(x) = 0 \quad (13)$$

where $D_{e,\text{Si}}$ and $\tau_{e,\text{Si}}$ are the diffusion coefficient and lifetime of minority electrons, respectively. Similar continuity equations exist for excess carriers in the other three neutral regions. The carrier generation rate per unit wavelength interval in each region is

$$G_{i,\lambda}(x) = \alpha_i(\lambda) F_{i-1}(\lambda) \exp[-\alpha_i(\lambda)(x - x_{i-1})], \quad x_{i-1} < x < x_i \quad (14)$$

where the absorption coefficient $\alpha_i(\lambda)$ at wavelength λ within region i is either $\alpha_{\text{Si}}(\lambda)$ or $\alpha_{\text{Ge}}(\lambda)$ available from Palik [26] and the flux of photons per unit wavelength interval at the boundary of each region ($x = x_i$) can be obtained as

$$F_i(\lambda) = F_{i-1}(\lambda) \exp[-\alpha_i(\lambda)(x_i - x_{i-1})] \quad (15)$$

Under the assumption of AR coating, the flux incident at the front surface ($x = x_0$) is given by

$$F_0(\lambda) = \frac{\lambda}{hc} I(\lambda) \quad (16)$$

where h is the Planck constant and c is the speed of light in free space.

The general solution to Eq.(13) for the density of excess minority holes per unit wavelength interval in the emitter region ($i=1$) is:

$$\begin{aligned} \Delta n_\lambda(x) = & A_1 \exp\left(\frac{x - x_0}{L_{e, Si}}\right) + B_1 \exp\left(-\frac{x - x_0}{L_{e, Si}}\right) \\ & + \frac{\alpha_{Si}(\lambda) F_1(\lambda) \tau_{e, Si}}{1 - \alpha_{Si}^2(\lambda) L_{e, Si}^2} \exp[-\alpha_{Si}(\lambda)(x - x_0)], \quad x_0 < x < x_1 \end{aligned} \quad (17)$$

where the diffusion length of minority holes $L_{e, Si} = \sqrt{D_{e, Si} \tau_{e, Si}}$, and the constants A_1 and B_1 are determined by boundary conditions that are related to the surface or interface recombination velocities S_i at $x = x_i$,

$$D_{e, Si} \left. \frac{d\Delta n_\lambda(x)}{dx} \right|_{x=x_i} = S_i \Delta n_\lambda(x_i) \quad (18)$$

The photocurrent density per unit wavelength interval that is collected at the depletion edge $x = x_1$ due to excess electrons generated by incident light at the wavelength λ , is

$$\begin{aligned} J_e(\lambda) = & e D_{e, Si} \left. \frac{d\Delta n_\lambda(x)}{dx} \right|_{x=x_1} \\ = & e \frac{D_{e, Si}}{L_{e, Si}} \left[A_1 \exp\left(\frac{x_1 - x_0}{L_{e, Si}}\right) - B_1 \exp\left(-\frac{x_1 - x_0}{L_{e, Si}}\right) - \frac{\alpha_{Si}^2(\lambda) F_1(\lambda) \tau_{e, Si} L_{e, Si}}{1 - \alpha_{Si}^2(\lambda) L_{e, Si}^2} \right] \end{aligned} \quad (19)$$

and that at the other depletion edge $x = x_2$ due to excess holes $\Delta p_\lambda(x)$ is

$$\begin{aligned} J_h(\lambda) = & -e D_{h, Si} \left. \frac{d\Delta p_\lambda(x)}{dx} \right|_{x=x_2} \\ = & -e \frac{D_{h, Si}}{L_{h, Si}} \left[A_3 - B_3 - \frac{\alpha_{Si}^2(\lambda) F_2(\lambda) \tau_{h, Si} L_{h, Si}}{1 - \alpha_{Si}^2(\lambda) L_{h, Si}^2} \right] \end{aligned} \quad (20)$$

where e is the electron charge.

Since the electric field inside of the depletion region ($x_1 < x < x_2$) is high, we can assume that the photogenerated carriers are swept out of the depletion region and are collected before any recombination takes place, thus the photocurrent density collected from the depletion region is

$$J_d(\lambda) = e[F_2(\lambda) - F_1(\lambda)]. \quad (21)$$

The total photocurrent density for the top Si cell should then be integrated across the entire solar spectrum as

$$J_{\text{photo}} = \int [J_h(\lambda) + J_e(\lambda) + J_d(\lambda)] d\lambda. \quad (22)$$

Neglecting the series resistance from Ohmic loss and the shunt resistance from leakage currents, we can calculate the net current density of the PV cell under the operating voltage V_{Si} as

$$J = J_{\text{photo}} - J_s \left[\exp\left(\frac{eV_{\text{Si}}}{kT}\right) - 1 \right] \quad (23)$$

where J_s is the reverse saturation current density of the Si junction with the junction voltage V_{Si} . A similar expression can be obtained for the bottom Ge junction. We first design a structure that satisfies the current-matching condition at zero bias under solar irradiance by varying the thicknesses of Si and Ge layers as well as junction depths in them. The structure described above in Fig.6 provides such current matching. At each bias, the voltage is divided between three regions, the Si-junction V_{Si} , the Si-Ge tunnel junction V_t , and the Ge-junction V_{Ge} as

$$V = V_{\text{Si}} + V_{\text{Ge}} - V_t. \quad (24)$$

The voltages V_{Si} and V_{Ge} are such that the currents flowing through both junctions are equal. The tunneling junction voltage V_t is the bias necessary to pass the solar currents generated in the two junctions; it reduces the total voltage across the tandem PV cell, and depends on the passing current. The negative impact of V_t can be neglected during “standard” irradiance of the tandem cell or when the solar concentration is low, in which case the tunnel junction can be treated as a perfect conductor between the two junctions ($g = \infty$, $V_t = 0$). But V_t ’s impact is obviously more severe under high concentration of solar irradiance and should be included in the simulation. The tunnel junction in this cell is expected to work in the forward direction with its voltage below the peak voltage V_p at which the tunneling current reaches its first peak I_p before it enters into the negative resistance region. In this region, the tunneling current density can be approximated by a linear relationship $J_t = gV_t$ characterized by the conductance per unit area g whose effect is basically to increase the series resistance of the solar cell. The conductance parameter for the hetero Si-Ge tunnel junction is unknown and is currently being studied. A series of experimental samples formed by bonding a heavily doped n+ Si membrane onto a heavily doped p+ Ge substrate have yielded high-quality structures with defects confined at the Si-Ge interface. Tunneling behavior of the bonded Si/Ge is emerging in electrical characterization [27]. It is therefore feasible to produce Si-Ge tandem PV cells with top and bottom junctions free of misfit dislocations even though Si and Ge have a large lattice mismatch. Defects confined at the Si-Ge interface will not degrade the performance of either junction, and under forward bias these defects will serve as recombination centers for excess carriers that will increase the tunneling current. That increase can increase g – a potential advantage for the solar cell because it reduces the voltage drop across the tunnel junction. We have included such an effect in the simulation by considering a range of $g > 100/\Omega\text{cm}^2$ - a value well exceeded by the Ge tunnel diode [28].

Other parameters that have been used in the calculation are as follows. The Si and Ge absorption data are taken from Palik [26], and the diffusion coefficients for electrons and holes are taken as properties of elemental Si and Ge [29]; these are respectively, $D_{e,\text{Si}} = 39.0 \text{ cm}^2/\text{s}$, $D_{h,\text{Si}} = 11.7 \text{ cm}^2/\text{s}$, $D_{e,\text{Ge}} = 101.4 \text{ cm}^2/\text{s}$, and $D_{h,\text{Ge}} = 49.4 \text{ cm}^2/\text{s}$. All minority carrier lifetimes are assumed to remain at $1 \text{ }\mu\text{s}$ for the range of solar power under consideration. The surface recombination velocities are 10^4 cm/s at the front side where the metal fingers are used for contact, and ∞ for the backside where a metal sheet is used for contact.

II.4 Results and discussion

We have calculated the current-voltage (I-V) characteristic and efficiency of the PV cell using the above parameters. The results are shown in Fig. 7 for the AM1.5G solar irradiance under 500 Suns which is chosen to show the impact of voltage across the tunnel junction. While there are no differences in the short-circuit current I_{sc} and open-circuit voltage V_{oc} , the fill factor reduces to $FF = 0.74$ with $g = 100/\Omega\text{cm}^2$ from 0.83 when such a voltage is neglected ($V_t = 0$). The short-circuit current and open-circuit voltage extracted from I-V characteristics are shown for Sun concentrations ranging from 1 to 1000 in Fig.8 where I_{sc} follows the solar power linearly; V_{oc} increases more rapidly from 0.9 V to 1.13 V in the 1 to 100 sun range, then slowly saturates as the concentration further increases. Both quantities show little dependence on the intensity of solar irradiance. But the fill factors are quite different for a range of the unit-area conductance g of the tunnel junction. When the series resistance of the PV cell is neglected, the fill factor increases slightly with the Sun concentration if the voltage across the tunnel junction is ignored. However, such a trend can be reversed when the limited conductance of the tunnel junction is taken into account. But for as long as the tunnel junction maintains a reasonable conductance of $g > 10^3/\Omega\text{cm}^2$, the fill factor remains roughly unchanged throughout the 1-1000 range of suns concentration and is consistently above 0.8.

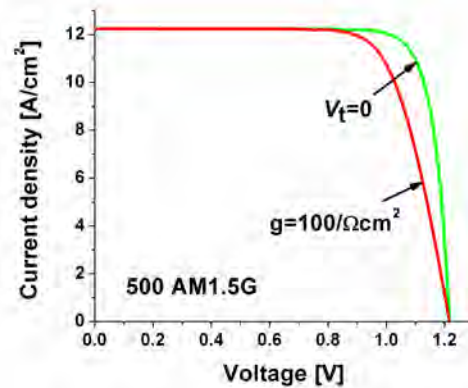


Figure 7. I-V characteristics at 500 suns of AM 1.5G solar irradiance for $V_t = 0$ and $g = 100/\Omega\text{cm}^2$.

Figure 9 shows our main result – maximum efficiency as a function of AM 1.5G solar-irradiance concentration for the c-Si on c-Ge tandem solar cell depicted in Figure 6. For comparison, we have also simulated a 100- μm -thick all-Si single-junction solar cell with the same doping profile as the Si region in the tandem cell. The Si cell has a 1- μm -thick “emitter”

region and a 99- μm “base” region. The all-Si maximum efficiency is also shown in Fig. 9. Clearly, the tandem cell consistently delivers higher efficiency than the Si single-junction cell throughout the 1-1000 range of the suns concentration even for $g = 100/\Omega\text{cm}^2$ which can be easily exceeded by a reasonably good tunnel junction. For a modest tunnel junction with $g = 1000/\Omega\text{cm}^2$, the efficiency increases from 19 % to 28 % as the sun concentration increases from 1 to 1000. In comparison with the all-Si single-junction solar cell, Si/Ge is 14 % better at 1 sun, and the Si/Ge improvement exceeds 20% at 50 suns, and reaches 23% at 200 suns and beyond.

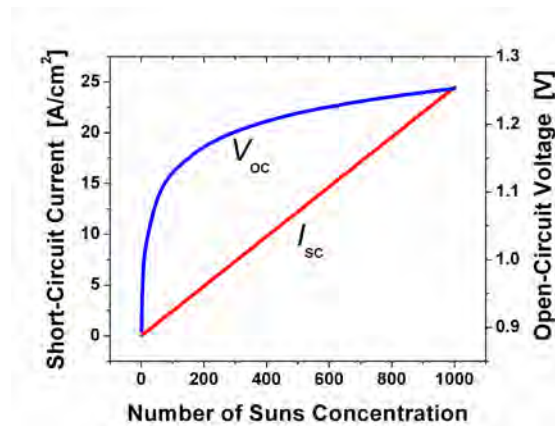


Figure 8. Open-circuit voltage and short-circuit current vs. number of suns concentration.

The fabrication of c-Si on c-Ge solar cells faces challenges. The Si/Ge solar cells are expected to have defects due to the large lattice mismatch between Si and Ge. The defect density will depend upon the method of cell preparation such as bonding a thin Si membrane to Ge or depositing Si on Ge via CVD. These defects can be localized at the Si/Ge interface or will exist in the form of threading dislocations. The former may not necessarily degrade the performance of the solar cell since the effect of defects only impacts the tunneling diode at the Si-Ge interface where defects serve as carrier-recombination centers that facilitate the tunneling current. However, threading dislocations will degrade the cell performance by creating additional recombination centers that decrease the lifetime of minority carriers both inside and outside of the pn-junction depletion region, resulting in smaller photo-current and larger dark current. It is therefore important to develop a method of fabrication that can effectively confine defects at the Si-Ge interface without allowing them to propagate into the active regions of either the Si or Ge layers.

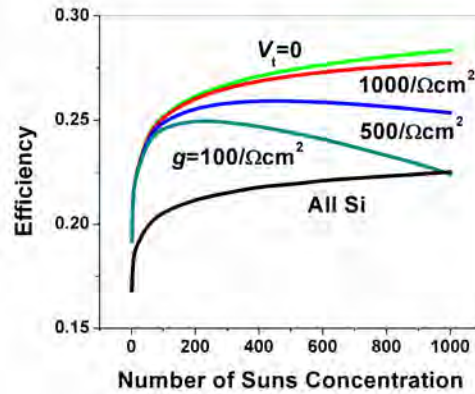


Figure 9. Efficiency of c-Si on c-Ge tandem PV cell vs. number of suns concentration for a range of the unit-area conductance of the tunnel junction. Also shown is the efficiency of an all-Si single junction PV cell of the same total thickness for comparison.

II.5 Conclusions

In conclusion, we have proposed and analyzed a thin-film c-Si on c-Ge tandem PV cell. The structure is $\sim 100\text{-}\mu\text{m}$ thick. Thicknesses of the various regions including junction depth are chosen such that the photocurrent-matching condition is satisfied. We have simulated tandem performance during standard AM1.5G solar irradiance with solar intensity ranging from 1 to 1000 suns. A general finding is that efficiency is optimized when the overall film thickness consists mainly of elemental Ge. We calculated efficiency for flat planar cells, assuming an AR coating on the front surface and no light-trapping enhancements such as texturizing or corrugating of the cell surfaces. We found that while the short-circuit current increases linearly with solar power, the open-circuit voltage increases super-linearly from 1 to 100 suns and then slowly saturates. The efficiency increases from 19 % to 28 % as the sun concentration increases from 1 to 1000. As a benchmark, we also calculated the efficiency of a $100\text{-}\mu\text{m}$ all-Si PV cell having the same parameters as the Si layer in the tandem structure. In comparison, the tandem c-Si on c-Ge PV cell delivers 14 % more efficiency during standard AM1.5G solar irradiance. That improvement grows to 23 % at 200 suns and beyond.

In this paper, we did not analyze and discuss the manufacturability of this Si/Ge cell, but we do recognize that economic and materials-science challenges must be met in order to realize the theoretical efficiencies in practical, large-area, cost-effective solar panels. The challenges are: attaining crystallinity, confining lattice-mismatch-induced defects at the Si-Ge interface, passivating the front surface, creating AR coating at the front surface, and doing all of the above at low cost including the Ge material costs. Looking to future experimental investigation of Si/Ge PV modules for solar panels, if it turns out after developmental effort that it will cost “too many dollars per watt” to produce large-area solar panels, then there is an excellent alternative “small-area approach” in which a large-scale array of small-area Si/Ge cells is deployed at the focus of a large solar-concentrator array. Also, it should be quite feasible to manufacture small-area Si/Ge PV cells for a host of “high value” applications in space platforms, airplanes and man-portable platforms.

To obtain group-IV performance that is improved over Si/Ge, the tandem's Si- junction layer can be replaced by a group-IV alloy whose bandgap is wider than that of Si. For example, the top junction could be cubic germanium carbide with a bandgap of approximately 1.8 eV. According to detailed-balance theory, this 3C GeC-upon-Ge PV would have efficiency of more than 30 %.

III. Field enhancement by coupled metal nanoparticles

III.1 Brief overview

The collective oscillations of free-electrons in the metal called surface plasmons (SPs) are known to induce strong localized electric fields near the surface of nanostructured metals whose intensities exceed that of the average fields impinging on the structure by orders of magnitude. This phenomenon had been used to demonstrate spectacular enhancement of sensitivity in Raman sensing as well as in fluorescence measurements [30,31], and had been proposed as a method to increase the efficiency of solar cells [32], detectors [33], and various nonlinear optical devices. We have previously developed an analytical model for isolated metal nanoparticles that not only reveals the origin of the optical enhancement but also allows for optimization of the nanoparticle structure in order to maximize the enhancement effect [34-36]. One limiting factor has been the contradicting requirement on a single sphere that needs to be simultaneously a good resonator and an efficient antenna. This difficulty can be resolved with the use of two or more coupled metal nanoparticles. Building upon our earlier work on isolated metal nanoparticles, we develop an analytical model for complex metal nanostructures where the coupling between the SP modes of different metal spheres can result in further enhancement. We show that the field enhancement for the isolated sphere is proportional to the Q -factor of the metal, but for two closely coupled spheres, it is proportional to Q^2 .

III.2 Theory of enhancement

The geometry of a single metal nanosphere with a radius a being placed in a dielectric media with the dielectric constant ϵ_D is shown in Fig.10(a) where the spherical polar coordinate system with the z -axis parallel to the dipole polarization is used. In the absence of external fields and charges, the electric potential of the eigen modes under the electro-static approximation should satisfy the Laplace equation $\nabla^2 \Phi = 0$ whose solution for the l -th mode can be given as [35,37]

$$\Phi_l = \begin{cases} \frac{a}{l+1} E_{max,l} \left(\frac{r}{a}\right)^l P_l(\cos \theta), & r < a \\ \frac{a}{l+1} E_{max,l} \left(\frac{a}{r}\right)^{l+1} P_l(\cos \theta), & r \geq a \end{cases} \quad (25)$$

where $P_l(\cos \theta)$ is the Legendre polynomial and $E_{max,l}$ is the maximum field just outside of the metal sphere at $r = a$ and $\theta = 0$. The continuity of the normal component of the electrical displacement $D_r = -\epsilon \frac{\partial \Phi_l}{\partial r}$ yields that the mode frequency $\omega_l = \omega_p \sqrt{\frac{l}{l+(l+1)\epsilon_D}}$, where ω_p is the metal Plasmon frequency. The mode frequency ranges from $\hbar\omega_1 = 1.967$ eV to $\hbar\omega_\infty = 2.261$

eV for Au nanosphere embedded in GaN ($\epsilon_D = 5.8$). The surface charge density related to the normal component of the electric field can be determined to be $\sigma_l(\theta) = \frac{2l+1}{l+1} \epsilon_0 E_{max,l} P_l(\cos \theta)$ where ϵ_0 is the permittivity of free space. Such a charge distribution on the metal surface produces dipole moment that vanishes for all higher order modes ($l \geq 2$), except the $l = 1$ mode whose dipole $p_1 = 2\pi a^3 \epsilon_0 E_{max,1}$. This dipole mode is the only solution coupled to the external fields for as long as the nanosphere diameter is much smaller than the wavelength, while all higher order modes remain uncoupled to external radiation modes. As a result, this dipole mode decays radiatively at a rate proportional to the sphere volume, $\gamma_{rad} = \frac{2\omega}{3\epsilon_D} \chi^3$, in which $\chi = \frac{2\pi a}{\lambda_D}$ is the metal sphere radius normalized to the wavelength λ_D in the dielectric corresponding to the excitation frequency ω . Simultaneously, all the modes also experience nonradiative decay due to the imaginary part of the metal dielectric function at roughly the same rate equal to the metal loss, $\gamma_{nr,l} \approx \gamma$.

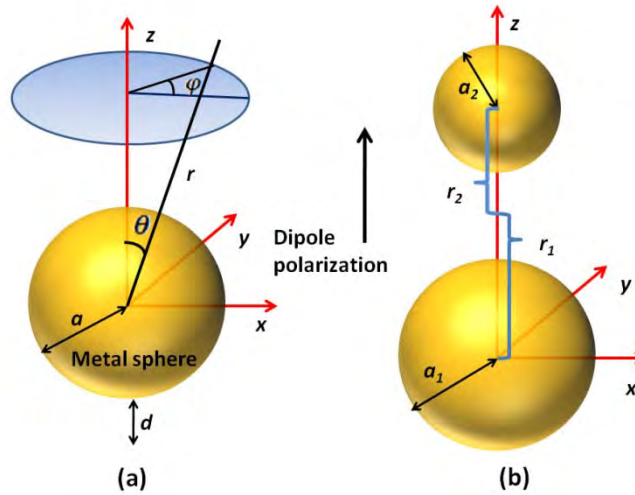


Figure 10. Illustration of (a) the spherical coordinate system used to describe the metal sphere dipole polarized along z -axis and (b) the geometry of two coupled metal spheres that are separated by $r_0 = r_1 + r_2$.

The effective volume $V_{eff,l}$ of the l -th mode can be defined through the mode energy that can be evaluated as an integral over the sphere surface $U_l = \frac{1}{2} \oint \Phi_l \sigma_l d^2 r = \frac{1}{2} \epsilon_0 \epsilon_D E_{max,l}^2 V_{eff,l}$ [38], from which we obtain $V_{eff,l} = \frac{4\pi a^3}{(l+1)^2 \epsilon_D}$. This mode volume is always less than the volume of the nanosphere and decreases with $(l+1)^{-2}$ as the SP energy gets concentrated in a very small volume close to the surface of the nanosphere and is contained within a narrow angle around axis z .

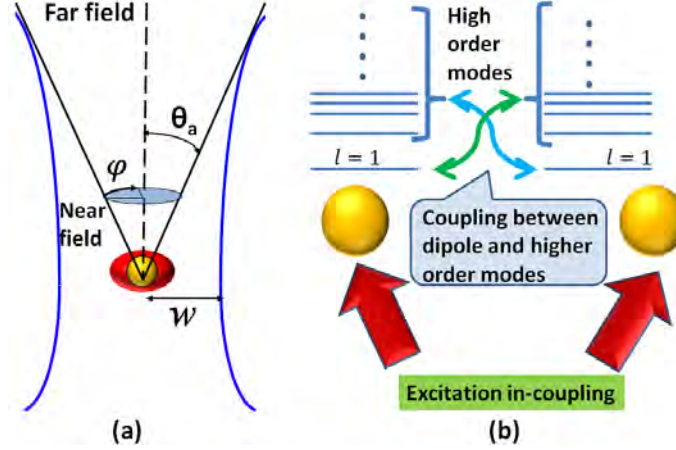


Figure 11. Illustration of (a) a metal nanosphere placed at the apex of a focused Gaussian beam with a numerical aperture characterized by the far-field half angle θ_a , and (b) the coupling of optical excitation into the dipole modes of both spheres and their subsequent coupling into the higher order modes.

We shall now evaluate the field enhancement by a single isolated metal sphere and then expand the model to obtain improvement with the use of coupled metal spheres. A fair comparison should be made with respect to a tightly focused light beam in the absence of metal spheres. Therefore we consider now a Gaussian beam with a numerical aperture characterized by a far field half angle θ_a gets focused onto a diffraction limited spot at the apex of the cone whose radius at the waist $w = \frac{\lambda_D}{\pi\theta_a}$ as shown in Fig. 11(a) (The polarization has been rotated by $\pi/2$ relative to Fig.10) [39]. The field in the focal spot E_{foc} is related to the power $|s_+|^2$ carried by the incident wave as $|s_+|^2 = \frac{\sqrt{\epsilon_D}}{Z_0} \pi \left(\frac{w}{2}\right)^2 E_{foc}^2$ where Z_0 is the impedance of free space. In the presence of a metal sphere, the incident light can be coupled into the dipole mode ($l = 1$) but not the higher order modes because all $l \geq 2$ modes have vanishing dipole moments and are not coupled with external fields. This is a process reciprocal to the radiative decay of the dipole mode into the free space radiation modes. The in-coupling coefficient κ_Ω can be shown to be related to the radiative decay rate γ_Ω of the dipole mode into the cone with a solid angle Ω as $\kappa_\Omega = \sqrt{\gamma_\Omega} \approx \frac{\theta_a}{2} \sqrt{\frac{3\gamma_{rad}}{2}}$ [34]. Now we arrive at the rate equation for the amplitude $A_1 = \sqrt{U_1}$ of the dipole mode as

$$\frac{dA_1}{dt} = j(\omega - \omega_1)A_1 - \frac{\gamma_{rad} + \gamma}{2}A_1 + \kappa_\Omega s_+. \quad (26)$$

At steady state, we obtain the field enhancement factor at a distance d (normalized $\chi_d = 2\pi d/\lambda_D$) from the metal sphere [34]

$$F_S = \left| \frac{E_{max,1}}{E_{foc}} \right| \left(\frac{a}{a+d} \right)^3 = \frac{\sqrt{2}}{\sqrt{[Q^{-1} + 2\chi^3/3\epsilon_D]^2 + \delta^2}} \left(\frac{\chi}{\chi + \chi_d} \right)^3 \quad (27)$$

where the Q -factor $Q = \frac{\omega}{\gamma}$ and the normalized excitation detuning $\delta = 2(1 - \omega_1/\omega)$. In the case of small sphere size, $Q^{-1} \gg \chi^3$, $F_s \approx \sqrt{2}Q \approx 14$ for $Q \approx 10$ for an Au sphere surrounded by GaN dielectric, when evaluated near sphere surface $\chi_d \ll \chi$ at resonance $\omega = \omega_1$. Actual field enhancement will be far less (see insert in Fig. 13). It is clear that in the case of isolated metal nanoparticles the higher order modes ($l \geq 2$) capable of concentrating their energies in small mode volumes while not subject to radiative decay play no role in enhancing the electric field simple because they do not couple well to the external field. At the same time, the dipole mode ($l = 1$) does couple to the outside rather well, but its effective volume is relatively large and thus its field enhancement cannot be all that high. It is obviously desirable to have the dipole mode act as an efficient antenna and higher order modes as efficient resonators. Unfortunately, the different SP modes of an isolated symmetric structure are orthogonal and decoupled from one another, thus a single sphere cannot be both a good resonator and an efficient antenna. This contradiction can, however, be resolved with the use of two or more closely spaced metal nanoparticles where the dipole mode of one sphere is coupled with the high order modes of another to create the situation in which efficient antennas are coupled with the resonators with high confinement. Based on the analytical model for the isolated metal nanoparticle, we develop a coupling theory that takes into account the energy transfer between the SP modes of closely spaced metal spheres. The theory can be applied to multiple spheres of different dimensions. But for simplicity, we examine exclusively the case of two spheres of equal size where the dipole modes of both spheres act as antennae and the superposition of higher order modes act as resonators allowing efficient coupling of the radiation into the gap region of the two coupled spheres. The coupling energy between the two modes can be obtained as an integral of the electric potential $\Phi_k^{(1)}$ of the l_1 -th mode of sphere 1 multiplied by the surface charge density $\sigma_l^{(2)}$ of the l_2 -th mode of sphere 2 evaluated over the surface of the sphere 2,

$$U_{l_1 l_2}^{(12)} = \oint \oint \Phi_{l_1}^{(1)} \sigma_{l_2}^{(2)} ds^{(2)} = -4\kappa_{l_1 l_2}^{(12)} A_{l_1}^{(1)} A_{l_2}^{(2)} \quad (28)$$

where $A_l^{(i)}$ is the amplitude of the l -th mode in the i -th sphere. Of all the coupling coefficients $\kappa_{l_1 l_2}^{(12)}$ we are mostly interested in the coupling between the dipole mode ($l = 1$) in one sphere and all the modes with index l in the other sphere $\kappa_{1l}^{(12)}$ because they are the only ones associated with energy transfer between antennae and resonators, which can be obtained analytically as $\kappa_{1l}^{(12)} = \frac{l+1}{2} \left(\frac{a_1}{r_0}\right)^{3/2} \left(\frac{a_2}{r_0}\right)^{l+1/2}$. The coupling between higher order modes of two spheres only shifts the resonant frequencies of those modes by a small amount, typically smaller than broadening γ and can be neglected in this analysis.

A rate equation similar to Eq.(26) can be established for the amplitude of each mode with additional terms that take into account of the coupling between the dipole mode in one sphere and all the modes in the other. At steady state, the total electric field at the location $r_1 = r_0 - r_2$ in the gap (Fig.10(b)) is the summation of all modes from both spheres as

$$\begin{aligned}
E(r_1) = & E_{max,1}^{(1)} \left[\left(\frac{a_1}{r_1} \right)^3 + \sum_{l=2}^{\infty} \frac{\omega_{1l} \kappa_{1l}^{(12)}}{(\omega_l - \omega) + j \frac{\gamma}{2}} \frac{l+1}{2} \left(\frac{a_1}{r_2} \right)^{3/2} \left(\frac{a_2}{r_2} \right)^{l+1/2} \right] \\
& + E_{max,1}^{(2)} \left[\left(\frac{a_2}{r_2} \right)^3 + \sum_{l=2}^{\infty} \frac{\omega_{1l} \kappa_{1l}^{(21)}}{(\omega_l - \omega) + j \frac{\gamma}{2}} \frac{l+1}{2} \left(\frac{a_2}{r_1} \right)^{3/2} \left(\frac{a_1}{r_1} \right)^{l+1/2} \right]
\end{aligned} \tag{29}$$

where $\omega_{1l} = \sqrt{\omega_1 \omega_l}$. The first term is the combination of the dipole mode of sphere 1 and the higher order modes of sphere 2, and the energy of all these modes is coupled in through the $l = 1$ mode of sphere 1, and vice versa for the second term. The field enhancement factor in the gap of two coupled spheres can then be obtained

$$\begin{aligned}
F_C = \left| \frac{E(r_1)}{E_{foc}} \right| = & \frac{\omega}{\sqrt{2} |M_{2 \times 2}|} \times \\
& \left| (m_{22} - m_{12}) \left(\frac{a_1}{r_1} \right)^3 \left[1 + \frac{1}{4} \frac{a_2 r_1^3}{r_0^2 r_2^2} \sum_{l=2}^{\infty} \frac{\omega_{1l} (l+1)^2}{(\omega_l - \omega) + j \frac{\gamma}{2}} \left(\frac{a_2^2}{r_0 r_2} \right)^l \right] \right. \\
& \left. + (m_{11} - m_{21}) \left(\frac{a_2}{r_2} \right)^3 \left[1 + \frac{1}{4} \frac{a_1 r_2^3}{r_0^2 r_1^2} \sum_{l=2}^{\infty} \frac{\omega_{1l} (l+1)^2}{(\omega_l - \omega) + j \frac{\gamma}{2}} \left(\frac{a_1^2}{r_0 r_1} \right)^l \right] \right|,
\end{aligned} \tag{30}$$

where the elements in the 2×2 matrix $M_{2 \times 2}$ are

$$\begin{aligned}
m_{11} = & j(\omega - \omega_1) + \sum_{l=2}^{\infty} \frac{\omega_{1l}^2 [\kappa_{1l}^{(12)}]^2}{j(\omega - \omega_l) + \frac{\gamma}{2}} + \frac{1}{2} \gamma_1^{(1)}, \quad m_{12} = j\omega_1 \left(\frac{a_2}{r_0} \right)^3 \\
m_{21} = & j\omega_1 \left(\frac{a_1}{r_0} \right)^3, \quad m_{22} = j(\omega - \omega_1) + \sum_{l=2}^{\infty} \frac{\omega_{1l}^2 [\kappa_{1l}^{(21)}]^2}{j(\omega - \omega_l) + \frac{\gamma}{2}} + \frac{1}{2} \gamma_1^{(2)}.
\end{aligned} \tag{31}$$

Here $\gamma_1^{(i)} = \gamma_{rad}^{(i)} + \gamma$ is the decay rate of the dipole mode of sphere i . Note the presence of different phases in the denominators – this is a direct consequence of delay associated with the energy transfer from one nanoparticle to another, i.e. the retardation effect. Therefore, this quasi-electric-static model is valid for as long as the dimensions of each individual particle are small compared to the wavelength, while the total size of the system of nanoparticles can be of the order of wavelength and even larger.

We shall now simplify Eq. (30) by examining the field enhancement by two equal spheres $a_1 = a_2 = a$ with zero gap $r_0 \approx 2a$. We use the fact that coupling coefficients and metal spheres are small such that $[\kappa_{1l}^{(i)}]^2 \approx 0$ for $l \geq 2$ and $Q^{-1} \gg \chi^3$, the strong coupling between the dipole modes causes the resonance ω_1 to split, $\frac{\omega_{\pm}}{\omega_1} \approx 1 \pm \sqrt{\kappa_{11}^2 - \frac{1}{4Q^2}}$.

We then realize that the terms from higher order modes ($l \geq 2$) in Eq. (30) are significant only for those lower indexes l whose frequency detuning from ω_1 is small, $Q^{-1} \gg 2(1 - \omega_l/\omega_1)$, we thus obtain at the lower split $\omega = \omega_-$, $F_C \approx 2\sqrt{2}Q \left| 1 - j \frac{9Q}{8} \right| \approx \frac{9\sqrt{2}Q^2}{4}$. In comparison with the field enhancement by a single metal sphere which is proportional to Q , we

now have additional contributions from higher order modes that have a relationship of Q^2 . We shall evaluate the enhancement in gaps greater than 2 nm since quantum effects such as electron tunneling and screening significantly reduce the enhancement when the gap is below 2 nm.

III.3 Results and discussion

The result is shown at mid gap in Fig. 12 for a range of gaps, $2 < g < 20$ nm at $\omega = \omega_1$, exhibiting a strong dependence on the sphere radius. It is not difficult to see that the mode coupling can shift the resonance, and in case of strong coupling, it splits into two resonances as shown in the insert of Fig. 12 where the frequency dependence of the enhancement at mid gap ($g = 5$ nm) with optimized radius of $a_{opt} = 33$ nm shows the peak occurs at a lower frequency $\omega < \omega_1$.

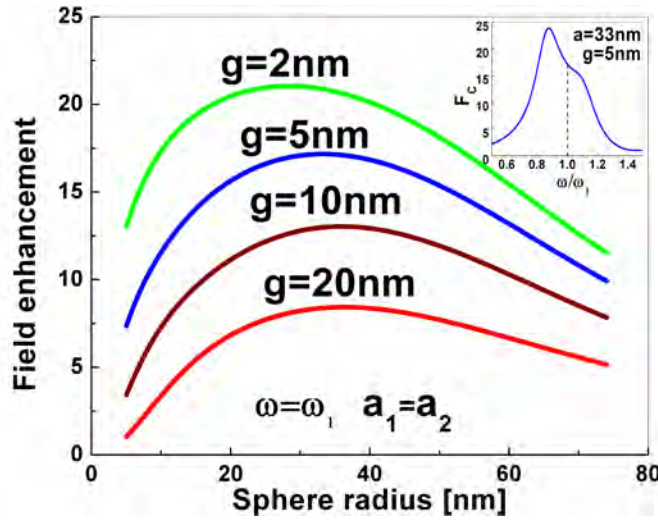


Figure 12. Field enhancement at the mid gap of two equal Au spheres in GaN vs. their radius at $\omega = \omega_1$. (Insert: frequency dependence of the mid-gap enhancement for the 5-nm gap with optimized sphere radius $a_{opt} = 33$ nm.)

Let us now compare the enhancement between single metal sphere and coupled spheres. To have a fair comparison, we obtain optimal enhancement for both cases at the locations of equal separation from metal surface. This means that for a single sphere we take the separation distance from its surface to be equal to half the gap, $d = g/2$, and we maximize the enhancement at optimal sphere radius at the dipole resonance, $\omega = \omega_1$, while in the case of coupled spheres, we not only optimize the radius of the two equal spheres but also the excitation frequency. Peak enhancement for the single sphere can be achieved by optimizing Eq. (27) at the normalized radius $\chi_{opt} = (3\epsilon_D\chi_d/2Q)^{1/4}$ to obtain $F_{S,opt} = \sqrt{2}Q/[1 + (2Q\chi_d^3/3\epsilon_D)^{1/4}]^4$ (see insert in Fig.13). The ratio of the optimal field enhancement between the two cases, $F_{C,opt}/F_{S,opt}$, is presented in Fig.13 where the frequency at which $F_{C,opt}$ is obtained is also shown. It can be stated that the enhancement in the gaps of coupled spheres always outperforms that of single spheres. The improvement over single sphere is about a factor of 2~3. This factor is substantially smaller than the factor of additional $9Q/4$ obtained in the limit of zero gap because of the resonance detuning of different modes and the presence of the gap. However, by

exploring multiple spheres of unequal dimensions, asymmetrical shapes, and off-center locations in the gaps, it is feasible to gain additional enhancement. For optical absorption and emission with properties directly proportional to the energy density, i.e. electric field squared (E^2), the improvement over single metal nanoparticles can be a factor of ~ 10 . For the surface enhanced Raman scattering (SERS) process whose intensity is proportional to E^4 , an additional factor of 100 can be recovered.

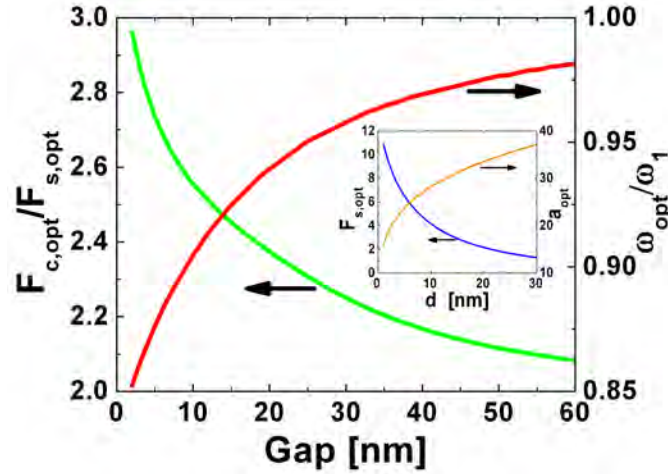


Figure 13. Ratio of optimal field enhancement by two coupled spheres to that by a single sphere, $F_{C,opt}/F_{S,opt}$, and the frequency shift ω_{opt}/ω_1 to yield $F_{C,opt}$ vs. the gap. (Insert: maximum enhancement by a single sphere $F_{S,opt}$ achieved at a_{opt} vs. separation equal to half gap $d = g/2$.)

In this work we have developed a rigorous analytical approach to the field enhancement in complex systems of coupled metallic nanoparticles. Our analysis confirms the fact that more complex metallic nanostructures do offer advantage over the single nanoparticles and provides a simple “engineering” explanation in which the large enhancement is achieved in a smaller “cavity” mode that is coupled to a larger “antenna” mode.

References

1. V.R. D'Costa, Y.-Y. Fang, J. Tolle, J. Kouvetakis, and J. Menéndez, *Thin Solid Films*, **518**, 2531 (2010).
2. R. A. Soref, J. Kouvetakis and J. Menendez, *Mater. Res. Soc. Symp. Proc.*, **958**, 0958-L01-08 (2007).
3. G. Sun, R. A. Soref, and H. H. Cheng, *J. Appl. Phys.* **108**, 033107 (2010).
4. J. Tolle, R. Roucka, V. D'Costa, J. Menendez, A. Chizmeshya, and J. Kouvetakis, *Mater. Res. Soc. Symp. Proc.* **891**, 0891-EE12-08 (2006).
5. G.-E. Chang, S.-W. Chang, and S. L. Chuang, *Opt. Express*, **17**, 11246 (2009).
6. Y.-H. Zhu, Q. Xu, W.-J. Fan, and J.-W. Wang, *J. Appl. Phys.* **107**, 073108 (2010).
7. G. Sun, H. H. Cheng, J. Menendez, J. B. Khurgin, and R. A. Soref, *Appl. Phys. Lett.* **90**, 251105 (2007).
8. R. A. Soref and C. H. Perry, *J. Appl. Phys.* **69**, 539 (1991).
9. H. P. L. de Guevara, A. G. Rodriguez, H. Navarro-Contreras, and M. A. Vidal, *Appl. Phys. Lett.* **91**, 161909 (2007).
10. M. Jaros, *Phys. Rev. B* **37**, 7112 (1988).
11. S. Adachi, *Properties of Group-IV, III-V, and II-VI Semiconductors*, (John Wiley and Sons, England, 2005)
12. V. R. D'Costa, C. S. Cook, A. G. Birdwell, C. L. Littler, M. Canonico, S. Zollner, J. Kouvetakis, and J. Menendez, *Phys. Rev. B* **73**, 125207 (2006).
13. V. R. D'Costa, C. S. Cook, J. Menendez, J. Tolle, J. Kouvetakis, and S. Zollner, *Solid State Commun.* **138**, 309 (2006).
14. J. Weber and M. I. Alonso, *Phys. Rev. B* **40**, 5683 (1989).
15. M. L. Cohen and T. K. Bergstresser, *Phys. Rev.* **141**, 789 (1966).
16. G. P. Agrawal and N. K. Dutta, *Long-Wavelength Semiconductor Lasers*, (Van Nostrand Reinhold Company Inc. New York, 1986).
17. Y.-Y. Fang, J. Xie, J. Tolle, R. Roucka, V. R. D'Costa, A. V. G. Chizmeshya, J. Menendez and J. Kouvetakis, *J. Am. Chem. Soc.*, **130**, 16095 (2008).
18. J. Poortmans and V. Arkhipov, *Thin film solar cells: fabrication, characterization and applications*, John Wiley & Sons LTD (2006).
19. R. Brendel, *Thin film crystalline silicon solar cells: physics and technology*, Wiley-VCH Verlag (2003).
20. Y. Hamakawa, *Thin-film solar cells: next generation photovoltaics and its applications*, Springer series in Photonics, (2004).
21. A. V. Shah and C. Droz, *Thin film silicon: photovoltaics and large-area electronics*, EFPL Press (2008).
22. G. Beaucarne, *Silicon thin film solar cells*, *Advances in Optoelectronics*, article 36970 Hindawi, (2007).
23. ASTM International, Designation G173-03, Standard tables for reference solar spectral irradiance: direct normal and hemispherical 37° tilted surface (2006)
24. K. Takahashi, M. Fujiu, M. Sakuraba and J. Muroto, 11th International Conference on Solid Films and Surfaces, Marseille, France, **212-13**, pp. 193-196 (2003).
25. M. A. Wistey, Y.-Y. Fang, J. Tolle, A. V. G. Chizmeshya, and J. Kouvetakis, *Appl. Phys. Lett.* **90**, 082108 (2007).

26. E. D. Palik, editor, Handbook of optical constants of solids, (Academic Press), vol. I (1985).
27. A. Kiefer, M. Lagally, W. Buchwald, and R. A. Soref, PCSI-37 37th Conference on the Physics and Chemistry of Surfaces and Interfaces (Santa Fe, New Mexico, January 2010).
28. D. Meyerhofer, G. A. Brown, and H. S. Sommers, Jr., Phys. Rev. **126**, 1329 (1962).
29. S. M. Sze, Physics of Semiconductor Devices, (Wiley, New York, 1981).
30. M. Moskovitz, *Rev. Mod. Phys.* **57**, 783 (1985).
31. S. Nie and S. R. Emory, *Science* **275**, 1102-1106 (1997).
32. S. Pillai, K. R. Catchpole, T. Trupke, and M. A. Green, *J. Appl. Phys.* **101**, 093105 (2007).
33. S. C. Lee, S. Krishna, and S. R. J. Brueck, *Opt. Express* **17**, 23160-23168 (2009).
34. J. B. Khurgin, G. Sun, and R. A. Soref, *Appl. Phys. Lett.* **94**, 071103 (2009).
35. J. B. Khurgin and G. Sun, *J. Opt. Soc. Am. B* **26**, B83-B95 (2009).
36. G. Sun, J. B. Khurgin, and C. C. Yang, *Appl. Phys. Lett.* **95**, 171103 (2009).
37. J. D. Jackson, *Classical Electrodynamics* (2nd Edition, John Wiley & Sons, New York 1962).
38. S. A. Maier, *Opt. Express* **14**, 1957-1964, (2006).
39. H. A. Haus, *Waves and Fields in Optoelectronics*, 1st ed. (Prentice-Hall, Englewood Cliffs, New Jersey, 1984).

List of Symbols, Abbreviations, and Acronyms

AM	Air mass
CMOS	Complementary metal–oxide–semiconductor
CVD	Chemical vapor deposition
CW	Continuous wave
DH	Double heterostructure
FTIR	Fourier transform infrared
HH	Heavy hole
IR	Infrared
LD	Laser diode
LH	Light hole
MQW	Multiple quantum well
PV	Photovoltaic
QW	Quantum well
SOI	Silicon-on-insulator
SP	Surface plasmon